Rolling Horizon Based Time-Triggered Distributed Control for AC/DC Home Area Power Network

Daud Mustafa Minhas ⬤, *Student Member, IEEE*, and Georg Frey ⬤, *Senior Member, IEEE*

Abstract—An energy-efficient smart home generally integrates renewable energy sources (RESs) with intelligent energy devices (IEDs) to make itself cost-efficient. However, the stochastic nature of the RESs and IEDs makes the power network uncertain, and it degrades the economic efficiency of the smart home. Hence a co-simulation based intelligent home energy management system (HEMS) is proposed in this article. It interconnects the rolling horizon-based model predictive energy scheduling mechanism with robust control strategies. It manages the load following energy supply entities (ESEs) optimally and efficiently. A time-ahead scheduler integrates an optimal algorithm to estimate the cost-optimal (e.g., minimizing total energy cost) decision signals for various ESEs by incorporating component based losses and efficiencies. Besides, a real-time distributed robust control strategy is established executing a coordinated energy sharing mechanism by incorporating an auxiliary power source. Time-triggered low-jitter wireless communication architecture is adopted to transfer the optimal decision signals from the central scheduler to the distributed device level local controller. A scenario based comparison of various ac/dc models of a home area power network evaluates the strength of the prospective HEMS.

Index Terms—Distributed control, energy optimization, power scheduling, time-triggered communication.

I. INTRODUCTION

NANO-GRID (NG) is a significant building block of a smart grid. It integrates various energy supply entities (ESEs), energy storage devices (ESDs), and intelligent energy devices (IEDs) within a single power network [1], [2]. Recently, a hybrid ac/dc NG configuration is introduced, that takes the advantage of both ac and dc configurations along with off-grid mode support [3], [4]. This configuration reduces the power conversion stages and provides an efficient integration of distributed energy resources (DERs) [5]. Since a hybrid NG is a complex power network, so the power management framework would also be obscure. The power management strategies based on the ISA-95

TABLE I
LIST OF ACRONYMS

Abbr.	Meaning	Abbr.	Meaning
AWGN	Additive white guassian noise	IEDs	Intelligent energy devices
DERs	Distributed energy resources	MPC	Model predictive control
ESDs	Energy storage devices	MPPT	Maximum power point tracking
ESEs	Energy supply entities	MILP	Mixed integer linear programming
GAS	Grid auxiliary storage	NG	Nanogrid
HAPN	Home area power network	QAM	Quadrature amplitude modulation
HEMS	Home energy management system	SNR	Signal to noise ratio
HBS	Home battery storage	VSI	Voltage source inverter

standard are widely adopted that consists of hierarchical control scheme [1]. This control scheme from bottom to the top includes primary (decentralized), secondary (centralized), and tertiary (global) control levels. However, in this article, the control levels are defined based on the execution time-frame of the control variables and the setting of the control loop [6]. The primary control architecture (e.g., the local controller requires local voltage values) allows the dispatchable device to act autonomously in balancing and securing the power network. It implements a grid forming robust control strategy to operate the overall system [7]. Whereas, the centralized secondary control mechanism (e.g., energy scheduler) is in charge of performing various optimization operations. It optimizes the energy flow, performing load demand and solar energy forecasting, economic dispatch, and power scheduling [2]. This control phenomenon usually predicts energy prices, power demands, and determines the amount of power that can be exchanged among various interconnected ESEs. A smart residential NG is also known as a home area power network (HAPN) comprised of various IEDs. Most of these IEDs are capable of being controlled and monitored wirelessly (e.g., internet of things devices). Real-time and accurate information exchange between controllers and IEDs is needed for efficient HAPN operations. The best candidate to implement such information sharing mechanism would be the wireless sensor and actuator networks [8]. advancement of communication technologies [8]. Distributed power systems are usually limited by the energy constraints and the data transmission bandwidth [9]. It is also beneficial to use the communication networks effectively and economically. In this regard, a significant contribution has already been made when a robust distributed control strategy based on communication was proposed to restore voltage and frequency under the condition of fixed time delay communication [10]. A discrete-time distributed communication scheme is presented in [11] that regulates the power flow and restoration of voltage/frequency during plug-and-play device operations. A continuous exchange of information between the distributed DERs is inefficient and

can lead to congestion [12]. The above literature describes the techniques of power-sharing that are continuously under stress due to the sharing of high volumes of data between controllers and IEDs resulting in frequent packet drops and increased delays [13]. There are two ways to reduce communication traffic; time-triggered and event-triggered communication strategies. As an event-triggered control, because of less control update, there is a little requirement for data transmission and computing power [9]. Furthermore, it is more resilient in supporting different configurations without making a new system design [14]. In the literature, several work has been reported on event-based control, e.g., primary local voltage control [15], frequency control [16]–[18], and optimum power flow control [19]. However, when more DERs are to be controlled, latency and jitter are more likely to occur [20]. Problems arise when several control loops have to be serviced. Lowering the latency in one control loop can affect the quality of the control signal of another control loop. Using the time-variant controller, a jitter correction is possible. However, it makes the algorithm more complex and involves additional functions of the system, such as timestamps [21]. On the other hand, time-triggered techniques improve predictability by lowering latency jitters and increase the performance [22]. Compared to event-triggered architectures, these often contribute to greater latency, but if all of the network's contributing nodes are aligned to a global time, then there is no jitter [8]. The time-triggered transmission is regulated by predefined time windows having a time division multiple access technique that leads to the benefit of a partial deterministic behavior during periodic services. Therefore, time-triggered communication is likely suitable for offline task scheduling in any control network. Hence, in this work, we adopt a time-triggered simplex communication approach to transfer decision signals from the scheduler to the device-level robust controller.

Moreover, the above literature identifies many of the major research problems at the microgrid level, and to the best of our knowledge, there are only a few HAPN-based studies. Moreover, the abovementioned literature did not address the solution strategies for hybrid ac/dc systems in HAPN that includes system losses, nor they achieved optimal cost minimization together with the equivalent energy sharing in both ac and dc subgrids. Besides, the energy scheduling among interconnected microgrids was achieved through the dc network or ac network to reduce the complexity of the energy flow. Mostly articles considered grid power flow as a single-controlled entity. While our work demonstrates two-staged scheduling and control framework as a distributive optimization strategy for minimizing power losses during power distribution.

A. Our Contribution

The fundamental entanglement of this article is to demonstrate a cost-optimal power-sharing phenomenon. To address the gaps in the literature review, and to demonstrate a new practical approach for optimized power flow in a smart grid, we propose a scenario of HAPN with a hierarchical control framework as
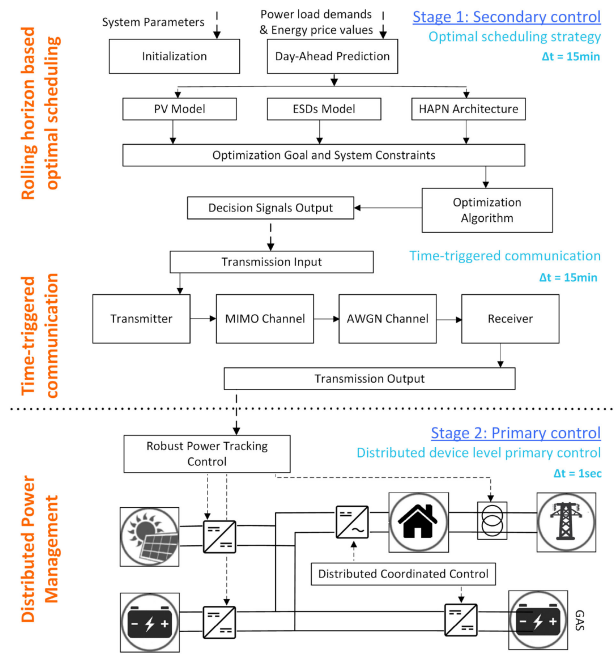

Fig. 1.   Proposed control strategy and system model.

shown in Fig. 1. This control hierarchy comprises of two fundamental control frameworks classified into stage 1; secondary control rolling horizon-based scheduler, and stage 2; primary distributed coordinated control. Both stages are interconnected with the help of wireless communication infrastructure.

At the first stage, the optimization problem of obtaining cost-optimal scheduling signals for various ESEs is discussed. Originally, the parameters associated with the optimization algorithm are initiated and execute a forecasting algorithm [23] to predict the future load demands and electricity price information. The analytical models for PV source, storage, and HAPN architecture are proposed here. These models further define the working rules and the system constraints, which increases the complexity of the power system under investigation. Also, it determines the convergence challenges for the proposed optimal algorithm. The scheduling decisions are optimized iteratively on a time-ahead basis for the receding horizon of 24-h. The optimal signals obtained from the scheduler are then transmitted to various IEDs installed at home through wireless transmission. To demonstrate a realistic communication phenomenon, we incorporate packet-based transmitter and receiver in our model. To make it more challenging, a multipath fading channel along with additive white Gaussian noise (AWGN) is introduced.

Whereas, at the second stage, a robust control strategy tracks down the signals received at the specific IED. It ensures the operation of the device according to the optimal decision values obtained from the scheduler. Hence, it always tracks the previously obtained values unless a new signal is received by the controller. Moreover, a distributed power-sharing phenomenon can also be observed at this stage by implementing a proportional energy sharing strategy involving energy reserves (in form of fuel cell, capacitor, or battery storage) for auxiliary operations

during grid disconnection, demand uncertainties, and scheduler signal loss.

This work is a significant extension of our earlier effort illustrated in [1]. Here, we optimize the overall cost of the energy and share the power more efficiently among various IEDs, considering an efficient low latency communication link and system inefficiency. In comparison to the previous works, the major contributions of this study include:

1) Introducing an extensive component-based novel hybrid ac/dc NG model for a HAPN. This model incorporates real operational constraints for the power supplied by conventional and renewable energy sources (RESs) at the home level. Besides, it incorporates the cost of battery life loss and the component-based cost of power losses during energy exchange among dc and ac subgrids. While previously, like in [24]–[26], the ac/dc power models were developed for higher-level distributed microgrids ignoring significant component's power losses.

2) Moreover, in comparison to [25], [27], [28], where only proportional power sharing was addressed. In this work, a novel two-stage co-simulation framework is adopted to implement multitime scale energy management and control strategy. First, an offline optimization scheduling strategy is proposed to minimize the total energy cost through an optimal dispatch of ac/dc hybrid NG. Second, a real-time coordinated power sharing mechanism is adopted to balance the power flow in the power network.

3) Previously suggested distributed event-triggering communication in [14], [17], and [26] depends only on local control data and local parameters. While in our work, a local robust controller tracks the optimal data obtained from the scheduler using time-triggered communication. However, we idealize a lossless communication between device-level control and the actuators. Our proposed time-triggered data transmission between the offline scheduler and the local controller will significantly reduce the transmission latency, jitter, and computing power associated with the communication by using the time stamp feature.

4) As compared to the conventional hierarchical control structure of microgrids [24]–[27], the proposed architecture is comprised of both secondary predictive control and primary distributed robust control layers. It improves the system predictability, redundancy and enables the plug-and-play feature in HAPN. The secondary control layer implements the analytical model of the HAPN, while the primary control layer is comprised of a current-controlled physical model of the HAPN components.

5) A performance comparison is made with some previous works (i.e., [3], [4], [24]) based on the inclusion of various types of losses and system topologies. Moreover, the impact of the hierarchical control framework on the stability and the economic operation of the ac/dc hybrid HAPN is thoroughly analyzed.

The rest of this article is organized as follows. In Section II, the problem formulation and system architecture are described that includes the individual components modeling, their efficiencies,

and the cost associated with these models. Section III presents multistag power scheduling and sharing control framework. It suggests the optimal and distributed control solutions using proposed HEMS schemes. A comparison case study is presented in Section IV followed by discussing the effects of communication failures and the uncertainties in the power network. Finally, Section V concludes this article.

II. PROBLEM FORMULATION AND SYSTEM ARCHITECTURE

The presented approach comprises of three-layer system architecture for hybrid ac/dc HAPN is shown in Fig. 1. It includes the optimal scheduling layer, cyber communication layer, and electrical physical layer integrating robust coordinated controller. The electrical physical layer includes the integration of the power distribution network and power electronic components. A physical device is connected to the scheduler through a cyber network from where it gets the reference power signal for its operation. The cyber layer allows the data from the scheduler to be shared with various power electronics converters. Moreover, an auxiliary energy reserve device (for emergency operations) is coordinated by a local energy sharing controller. This coordinated control is attached to the physical network via sensors and the actuators.

A. Model Dynamics for Energy Entities

1) Battery Storage Model: To demonstrate the cost-optimal solution of a storage system, a model is required that describes the overall power losses ($P_{b.\text{loss}}(t)$) associated with the storage system [2]. It may also includes the battery efficiency (η_b) and the efficiency (η_{con}) related to the converter attached to a battery

$$P_{b.\text{loss}}(t) = \begin{cases} (\eta_b^{-1}\eta_{\text{con}}^{-1} - 1)P_{b.dch}(t) = (\eta_{b.\text{con}}^{-1} - 1)P_{b.dch}(t) \\ (\eta_b\eta_{con} - 1)P_{b.ch}(t) = (\eta_{b.con} - 1)P_{b.ch}(t) \\ P_{b.self}(t), \qquad if\, P_{b.dch}(t) \; P_{b.ch}(t){=}0 \end{cases}$$
$$(1)$$

where discharging rate ($P_{b.dch}(t)$) is established when power is positive, and the charging rate ($P_{b.ch}(t)$) is established when power sign is negative.

In addition, the difference in energy levels ($E_b(\triangle t)$) of a battery during varying time slots ($\triangle t = t - (t - 1)$) depends on the battery charging, discharging rates, (dis)charging efficiency factor ($\eta_{b.con}$), and the battery self discharge ($P_{b.\text{self}}(t)$)

$$E_b(\triangle t) = \eta_{b.con}P_{b.ch}(t) - \eta_{b.con}^{-1}P_{b.dch}(t)$$
$$- P_{b.\text{self}}(t). \quad \forall t \in \{2\cdots T\}. \quad (2)$$

$E_b(t)$ also known as state of charge (SoC) that is the reciprocal of battery depth of discharge (DoD): $SoC = (1 - DoD)$. Whereas, the battery SoC is limited to its maximum $\overline{E}_b$ and the minimum $\underline{E}_b$ threshold

$$\underline{E}_b \leq E_b(t) \leq \overline{E}_b, \quad \forall t \qquad (3)$$

where $\underline{E}_b = (1 - DoD)\overline{E}_b$. Furthermore, $P_{b.ch}(t)$ and $P_{b.dch}(t)$ are also bounded by the maximum and minimum values at any time t, such as

$$\underline{P}_{b.ch} \leq x_{dc.b}P_{b.ch}(t) \leq \overline{P}_{b.ch}, \quad \forall t \qquad (4)$$
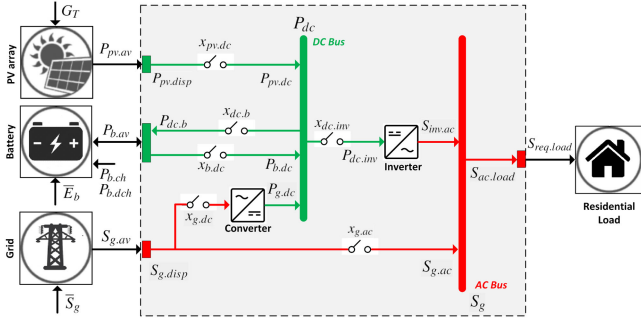
Fig. 2. HAPN architecture (Scheduler perspective).

$$\underline{P}_{b.dch} \leq x_{b.dc} P_{b.dch}(t) \leq \overline{P}_{b.dch}, \quad \forall t \qquad (5)$$

where $x_{dc.b} \in \{0,1\}$ and $x_{b.dc} \in \{0,1\}$.

2) Inverter Efficiency Model: The inverter acts as interconnecting converter to transfer power from the dc to the ac subgrid. There is loss of power inside the inverter in the form of heat. While transferring power, the inverter defines the phase angle of the current being injected into the ac line. The current transferred to the ac line is limited to upper threshold of the power $(\overline{S}_{inv.ac})$ handled by the inverter,

Hence, it is established that an inverter may experience power loss due to the power flow. This power can be from PV or the battery. However, if it is impossible then this power can be requested from the main grid. The self consumption of the inverter is determined by the inverter's efficiency data provided in the datasheets or by $\eta_{inv} = S_{inv.ac}/P_{dc.inv}$.

3) Energy Demands Model: We have used a day-to-day energy request profile of a single home already set up in [2]. The Center of Renewable Energy System Technologies develops this model. In this model, the power utilization information for the number of residents is gathered. It includes their everyday activities in the home and the probability of activating a certain appliance on the day of a week basis for the whole year [29].

B. HAPN Architecture

The HAPN architecture under consideration is shown in Fig. 2. The service grid line is connected directly to the HAPN's ac subgrid and via an ac/dc converter to the dc subgrid. PV-array and home battery storage (HBS) are coupled to the dc line directly using their built in dc/dc converters. The dc subgrid is further joined with ac line using a dc/ac inverter. Controllable switches are added in the system to implement the binary operational constraints in the NG.

1) Grid-Tie Line: It is assumed that the dispatched power $(S_{g.disp}(t))$ from utility grid is always lesser than the available power $(S_{g.av}(t))$. Whereas, the utility grid is upper bounded by its maximum threshold $\overline{S}_g$.

$$S_{g.disp}(t) \leq S_{g.av}(t) \leq \overline{S}_g. \quad \forall t. \qquad (6)$$

The power available from utility at ac subgrid $(S_{g.ac}(t))$ is

$$S_{g.ac}(t) = S_{g.disp}(t) - x_{g.dc}(t)\left(\eta^{-1}_{(ac/dc)} P_{g.dc}(t)\right), \quad \forall t \qquad (7)$$

where $x_{g.dc}(t) \in \{0,1\}$ and $\eta_{(ac/dc)}$ represents converter efficiency. The power available from utility grid at dc subgrid $(P_{g.dc}(t))$ is shown in (8); given that, $x_{g.ac}(t) \in \{0,1\}$.

$$P_{g.dc}(t) = \eta_{(ac/dc)}\left(S_{g.disp}(t) - x_{g.ac}(t)S_{g.ac}(t)\right). \quad \forall t \qquad (8)$$

2) PV-Array Connection: The dispatched power $(P_{pv.disp}(t))$ from PV-array is limited to the available power $(P_{pv.av}(t))$, which is always lesser than the maximum of power harvested by the PV $(\overline{P}_{pv}(t))$, because some of it is lost during the processing by maximum power point tracking (MPPT) algorithm.

$$P_{pv.disp}(t) \leq P_{pv.av}(t) \leq \overline{P}_{pv}(t), \quad \forall t \qquad (9)$$

given $x_{pv.dc}(t) \in \{0,1\}$. The power available from PV at dc subgrid is

$$P_{pv.dc}(t) = x_{pv.dc}(t)P_{pv.disp}(t), \quad \forall t. \qquad (10)$$

3) Battery Storage Connection: The NG integrates a battery acting as a storage and a buffer with available power $(P_{b.av}(t))$ limited by the capacity of the battery $(\overline{E}_b)$ such as

$$P_{b.av}(t) \leq \overline{E}_b. \quad \forall t. \qquad (11)$$

The power available from the battery at dc subgrid $(P_{b.dc}(t))$ during discharging is

$$P_{b.dc}(t) = \min\left[P_{b.dch}(t), P_{b.av}(t)\right] x_{b.dc}(t), \quad \forall t \qquad (12)$$

where $x_{b.dc}(t) \in \{0,1\}$. The power available from dc line to battery $(P_{dc.b}(t))$ is shown in (13), given that $x_{dc.b}(t) \in \{0,1\}$

$$P_{dc.b}(t) = \min\left[P_{dc}(t), P_{b.ch}(t), \overline{E}_b - P_{b.av}(t)\right], \quad \forall t \qquad (13)$$

where $(P_{dc}(t))$ is the power available at dc subgrid.

4) DC Subgrid Connection: The power exchanged at dc bus is

$$x_{g.dc}(t)P_{g.dc}(t) + x_{b.dc}(t)P_{b.dc}(t) + \ldots$$
$$x_{pv.dc}(t)P_{pv.dc}(t) = x_{dc.b}(t)P_{dc.b}(t) \ldots \qquad (14)$$
$$+ x_{dc.inv}(t)P_{dc.inv}(t), \quad \forall t$$

where $x_{dc.inv}(t) \in \{0,1\}$. Whereas, the further constraints applied at dc subgrid include: The battery's charge and discharge process can not take place concurrently

$$x_{b.dc}(t) + x_{dc.b}(t) \leq 1. \quad \forall t. \qquad (15)$$

DC subgrid cannot takes in the power from the grid at the time when it is transferring power toward ac subgrid through the inverter

$$x_{g.dc}(t) + x_{dc.inv}(t) \leq 1, \quad \forall t. \qquad (16)$$

The discharging of the battery and the power from the utility grid cannot be activated simultaneously

$$x_{b.dc}(t) + x_{g.dc}(t) \leq 1, \quad \forall t. \qquad (17)$$

5) AC Subgrid Connection: The power exchanges at ac subgrid is

$$x_{g.ac}(t)S_{g.ac}(t) + x_{dc.inv}(t)S_{inv.ac}(t) = S_{ac.load}(t), \quad \forall t \qquad (18)$$

where

$$S_{inv.ac}(t) = P_{dc.inv}(t) - P_{inv.loss} \forall t. \qquad (19)$$

Remark 1: The home occupants' comfort is further guaranteed by making the supply power always greater than the load demands i.e., $S_{\text{req.load}}(t) \leq S_{\text{ac.load}}(t)$.

C. Entities Cost Modeling

1) Battery Lifetime Loss Cost: Battery lifetime is usually expressed as number of storage life cycles given by the manufacturers. To obtain the storage life loss estimate, a generalized ampere-hour (Ah) life-cycle storage model is used. At each stage, the storage life loss ($L_f(t)$) is the ratio of the effective consumed power ($A_c = \lambda_{\text{SOC}}(t) \times A'c(t)$) to the total effective capacity ($A_{\text{total}} = \eta_{b.\text{con}} \times \overline{E}_b$) [30] and is shown as

$$L_f(t) = A_c / A_{\text{total}}. \quad \forall t. \quad (20)$$

The battery bank's effective consumed power depends on both the actual consumed power ($A'_c(t)$) and the storage's operating SoC level ($\lambda_{\text{SOC}}(t)$) as seen in [30]. Whereas the average productive capacity of any lead-acid battery is determined on the basis of data from deep-cycle lead-acid battery manufacturer [31]. That means, discharging battery at high SoC will increase the lifetime of the storage. The calculated $L_f(t)$ in (20) can be used to establish a lifetime loss cost for the battery state and is illustrated as

$$C_{b.l}(t) = L_f(t)C_{b,\text{ivt}}, \quad \forall t \quad (21)$$

where $C_{b.\text{ivt}}$ is the investment cost of the battery bank.

2) Grid Energy Pricing: In this article, a real-time pricing information is obtained from [32] to demonstrate the effectiveness of dynamic grid pricing schemes $C_g(t)$ for demand side management strategies in smart homes.

3) Inverter Power Cost: Inverter power is actually the power from battery, PV, and the losses induced by the inverter itself. So, the inverter power cost ($C_{\text{inv.ac}}(t)$) would be the operating cost of the battery (ϕ) and PV (φ) and is illustrated in (22). This operating cost per watt is a function of aggregated investment cost to the working cycle of the component.

$$C_{\text{inv.ac}}(t) = \varphi P_{\text{pv.dc}}(t) + \phi P_{b.\text{dc}}. \quad \forall t. \quad (22)$$

III. MULTISTAGE POWER SCHEDULING AND SHARING CONTROL FRAMEWORK

The HAPN is a single energy network that combines power in-feed from the electricity grid, photovoltaic arrays, residential energy storage. Additionally, it provides power at a fixed voltage standard to the residential appliances [33]. In this article, the energy allocation strategies and robust real-time power sharing mechanism are demonstrated by implementing a home energy management system (HEMS) integrating power scheduling and control strategies. Where, a primary control unit tracks down the reference signals obtained from the scheduler, and activates the devices accordingly. Furthermore, it compensates the voltage deviations during load uncertainties or grid disconnection. It activates distributed coordinated control for energy balancing mechanism using reserve emergency power source, which in our case is the grid auxiliary storage (GAS). GAS with energy
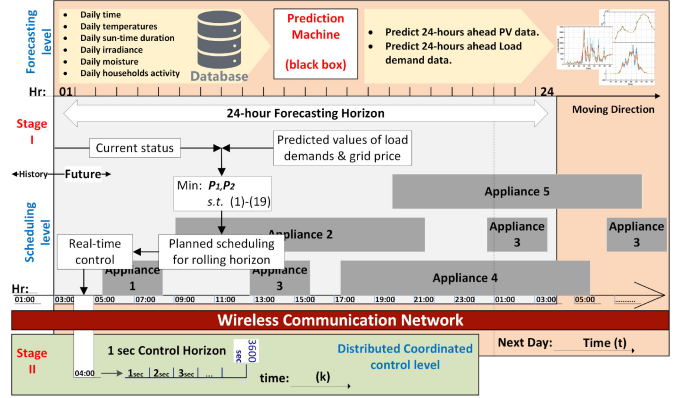

Fig. 3. Energy management system architecture.

status ($Egas(k)$) is responsible for supplying HAPN with ancillary services (i.e., assistance for island operation and power quality problems) [34]. With its dispersed organized control unit consisting of a proportional and integral control system, GAS power management monitors the disparity of the power network. It consumes the network's surplus capacity and provides power through power shortages.

A two-staged model predictive control (MPC) based scheduler and control infrastructure is proposed in Fig. 3. At the first step, an energy scheduler is installed at the secondary control level, which means that the net cost of generated energy is minimized. It combines a prediction module with an optimization algorithm that predicts the generation of time-ahead PV and the load requests of the customer. Whereas, an optimal algorithm optimizes the scheduling of ESEs, and generates the optimal decision signals in the form of device power set-points. These set-points are transmitted through a communication connection to the primary controller of the system.

In addition, a rolling-time horizon based forecasting and scheduling approach is proposed to reduce forecasting errors. This acts on a time scale of several minutes i.e., $t \in [1, 2, \ldots, T]$. Whereas a robust control power allocation method is implemented in the second level, operating at a time-scale of seconds, i.e., $k \in [1, 2, \ldots, k]$, and is based on coordinated energy sharing strategy. A system controller's robust control mechanism continuously monitors the received reference signal and thus regulates the activation of the device along with its power levels [1], [35].

The energy management strategy focused on two-stage scheduling and controlling mechanism is demonstrated in the following algorithm. A linear programming based algorithm is used to operate the scheduling strategy that takes the duration of the whole day into account and analyses the future knowledge of the resources and the load demands. The optimal values of the control variables are estimated using mixed integer linear programming (MILP) that minimizes the objective function illustrated in (23). As a result, the statistical horizon shifts to the next period in time and the whole process is repeated. The sampling time is chosen to be $t = 15\,\text{min}$ and the prediction horizon length is $T = 24\,\text{h}$.

Algorithm 1: Algorithm for Power Cost/Balance Reciprocity.

---

procedure Dynamic Scheduling & Control algorithm
System Initialization
Set parameter values
Set system bounds
Determine control variables initial values
for $(t \leq T - 1)$ **do**
Executing PV and load demand prediction strategy
Initialize system constraints
Initialize components constraints
while $\mathscr{P}1 \neq min(Cost)$ **do**
Executing optimal scheduling algorithm
end while
Store scheduling variables set $(\mathbf{u}_x^{\mathscr{D}}(1)$ & $\mathbf{u}_P^{\mathscr{D}}(1))$
Transmit decision signal to the device level controller
  through WLAN.
Initializing distributed robust control
for $(k \leq K - 1)$ **do**
Executing robust control scheme on received signals
Tracking and applying signals decisions set
  $(\mathbf{u}_x^{\mathscr{D}}(k)$ & $\mathbf{u}_P^{\mathscr{D}}(k))$
while $\mathscr{P}_2 \neq max(Balance)$ **do**
Executing coordinated control strategy for auxiliary
  power sharing
Integrate real-time control variable set
  $(\mathbf{u}_{ch}(k)$ & $\mathbf{u}_{dch}(k))$
end while
$k \leftarrow k + 1$
end for
$t \leftarrow t + 1$
end for
end procedure
Conclude total energy utilization cost
Conclude real-time balancing phenomenon
Conclude ESEs utilization factor and penetration level
Conclude EEs loss factor and loss cost

A. Rolling-Horizon Based Optimal Power Scheduling

The goal is to minimize the total cost of energy provided by the ESEs. This dilemma is conceived as a time-to-time energy scheduling problem, such as

$$\mathscr{P}_1 = \min_{\mathbf{u}_P^{\mathscr{D}}(t), \mathbf{u}_x^{\mathscr{D}}(t)} \sum_{t=1}^{T} \{C_g(t)(S_{g.\text{ac}}(t)$$
$$+ P_{g.\text{dc}}(t)) + C_{b.l}(t) + C_{\text{inv.ac}}(t)\}.$$
$$\text{s.t. } (1)-(19). \qquad (23)$$

The consumption of PV power has a focus in our control strategy. So, if it is unable to fulfill the load specifications, the battery power would be used. If required, the power can be fed from the grid. For any time frame t the power demands $(S_{\text{req.load}}(t))$ must be fulfilled by a variation of the ESEs. Besides, the problem can be solved under the influence of some security constraints already discussed in Section II.

A computational analysis of the problem to be assessed is addressed as follows. Considering a HAPN, which requires a collection of energy dispatchable entities $\mathscr{D} = \{1, 2, \ldots, n^D\}$ all associated with a single operating domain (Home). Let $u_P^{\mathscr{D}} \in \mathbb{R}_+$ be the power shared at time-slot $t \in \mathscr{T} = \{\tau, \ldots, \tau + T - 1\}$ by the particular energy entity and $u_x^{\mathscr{D}} \in \mathbb{R}_+$ is the entities' binary activation set. A subset of entities (i.e., grid power, load requirements) $\mathscr{D}_{\text{AC}}$ is attached to the HAPN ac line, while a tuple of generators (i.e., PV, HBS) $\mathscr{D}_{\text{DC}}$ is attached to the dc line. HEMS evaluates the objective functions set $\mathscr{P} : \mathbb{R}+ \mapsto \mathbb{R}+$, sets the electricity supply costs for households at time-slot t, and balances the power network at time-slot k.

1) Time-Triggered Communication Strategy: In this article, we establish a model of HAPN incorporating time-triggered WLAN 802.11ac high throughput communication link [36]. It also integrates an AWGN fading channel [37] to demonstrate the noise disturbances in the channel during transmission. Since the scheduler and the IEDs are in close proximity within a house, so apparently less noise and uncertainty in communication link is expected. We assume that the IEDs are in a stationary condition, and the communication between HEMS and IEDs is carried out in low-bandwidth simplex mode. This is a simple unidirectional time-triggered communication strategy that significantly reduces the unnecessary transmissions and bandwidth consumption, making effective utilization of the communication link. In this article, we demonstrate that the signals are transmitting periodically at equidistant sampling instants. As the time windows for all actions are predefined by the offline scheduling, the outcome is a time system with continuous latencies and no jittering. The delays are constant, meaning a global synchronization is realized, and there is no jitter. Regardless the number of IEDs are operating, each of these has its own dedicated time slots to communicate with the scheduler and the time invariant algorithms are used. MATLAB communication toolbox related to TCP/IP-specific identification, retransmission, as well as control of the queue length of the router using the algorithm of random early detection, and congestion avoidance are utilized for data transmission. The communication model has three main components:

a) Transmitter: It comprises of two main communication network layers including the data link layer and physical layer. Data link layer generates data and control information signals. It provides protocol and service information transfers between peer layers of communicating IEDs. A transmitter creates a physical layer convergence procedure service data unit and encodes the bits to create a single packet waveform. Besides, a quadrature amplitude modulation (QAM) technique is used for transmitting data.

b) Channel: Our WLAN model operates using an unlicensed radio frequency spectrum of 2.4 GHz, having a bandwidth of 20 MHz with maximum throughput up to 800 Mbps. WLAN channel bandwidth is defined to be 5 MHz.

c) Receiver: The working concept of a receiver is to recover a message from the transmitted packet. The receiver has two components: packet detection and packet recovery. The task the receiver has to implement including packet detection, time and frequency synchronization, carrier frequency offset correction,
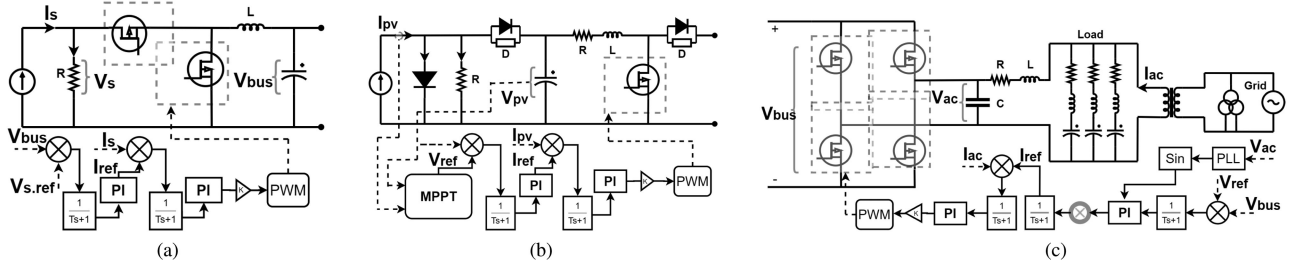
Fig. 4. HAPN components architecture (Primary robust control perspective).

MIMO channel estimation, received packet demodulation, and decoding the required data information.

B. Robust Power Tracking Control

1) ESDs Converter Control: The dc buck/boost converter attached to the ESDs usually supports the voltages level both at the storage side and as well as on dc subgrid side. The schematic of a converter and the associated control framework is shown in Fig. 4(a). The relevant control parameters associated with the converter are the output voltage on dc subgrid side is V_{bus} while on storage side is V_s and the current flowing through the converter is I_s. Whereas the control law for storage is based on conventional robust control strategy comprised of the outer voltage control loop and the inner current control loop. Both loops include proportional and integral (PI) controllers to track the reference voltage and current values, respectively [38]. The reference input voltage $V_{s.ref}$ is the voltage at which the dc subgrid operates.

2) PV Power Support Control: Fig. 4(b) presents the PV power converter topology and the control strategy to facilitate the flow of energy from the PV generator. The solar panels are attached to the dc subgrid using MPPT converter. The voltage across the terminals of the PV panel is represented as V_{pv}. Whereas V_{bus} is the output voltage and I_{pv} is the output current of the solar panel.

Practically, the voltage and the current values from the PV panel are feed to the MPPT controller, which in return gives out the reference voltage value to be controlled by the primary controller attached to the converter. The MPPT controller is based on the perturbation and observation method [38]. While the primary control strategy is comprised of a PI controller along with two-staged control loops, e.g., the outer voltage loop and the inner current loop. Through PI-based voltage controller the PV voltage V_{pv} is forced to follow the reference voltage value V_{ref} obtained from MPPT.

C. Distributed Coordinated Control for Energy Balancing

Due to the preplanned schedule or unplanned disruptions, the NG may work in off-grid operational mode. Therefore, reserve energy sources must also be used in voltage/current-controlled inverter (VSI) mode to provide fast voltage/frequency support. VSI may provide active and reactive power support for HAPN by compensating for a portion of the power required for voltage and frequency reconstruction. Here, the objective is to balance

the supply and demand within the HAPN. The dilemma is then formulated as a problem of real-time energy balancing and is demonstrated as

$$\mathscr{P}_2 = \min_{\mathbf{u}_{gas}(k)} \{ S_{g.ac}(k) + P_{g.dc}(k) + P_{pv.dc}(k) + P_{b.dc}(k)$$
$$+ \mathbf{u}_{gas}(k) - S_{ac.load}(k) - P_{dc.b}(k) \}, \forall k$$
$$\text{s.t.} \tag{24}$$
$$\underline{E}_{gas} \leq E_{gas}(k) \leq \overline{E}_{gas}, \quad \forall k$$
$$\underline{P}_{gas.ch} \leq \mathbf{u}_{gas}(k) \leq \overline{P}_{gas.dch}, \forall k$$

where $\mathbf{u}_{gas}(k) = [x_{gas}(k) P_{gas}(k)]$ is the control signal for activating auxiliary storage power ($P_{gas}(k)$). The available energy in a GAS is bounded by upper ($\overline{E}_{gas}$) and lower ($\underline{E}_{gas}$) energy thresholds. Although the charging and discharging rates of the storage are constrained at any time k by the maximum and minimum values as seen in (24).

1) Voltage Source Inverter Control: This section demonstrates the topology and the control schematic of the inverter. In this article, the power load is attached to the ac subgrid and the priority is given to the dc supply to fulfill the load requirements over the ac grid supply. To ensure the maximum transfer of power from the dc subgrid to the ac subgrid the voltages at the dc subgrid must be consistent. Due to which the inverter is continuously under stress. A voltage controlled VSI is implemented so that the unpredictable conduct of the sustainable power sources could be controlled. Fig. 4(c) shows a schematic of the grid-connected VSI and its control framework. As indicated, the outer voltage control loop determines the dc subgrid voltages for the inverter input. The voltage regulator fundamentally decides the magnitude of the current to be infused into the ac bus. While the dc bus voltage remains constant. PI controllers are generally used to actualize the voltage regulator [39].

The power shared by the GAS through VSI can be described as [26]

$$P_{gas} = v^{gd} i^{gd} + v^{gq} i^{gq}, \quad Q_{gas} = v^{gq} i^{gd} - v^{gd} i^{gq} \tag{25}$$

where i^{gd} and i^{gq} are the direct and quadrature components of the ac bus current I_{ac}, respectively, while v^{gd} and v^{gq} are the direct and quadrature components of the ac bus voltage V_{ac}, respectively. A d–q reference frame transition is adopted, which rotates with the common reference frequency (ω), applying VSI control. The idea is to reproduce the working concept of
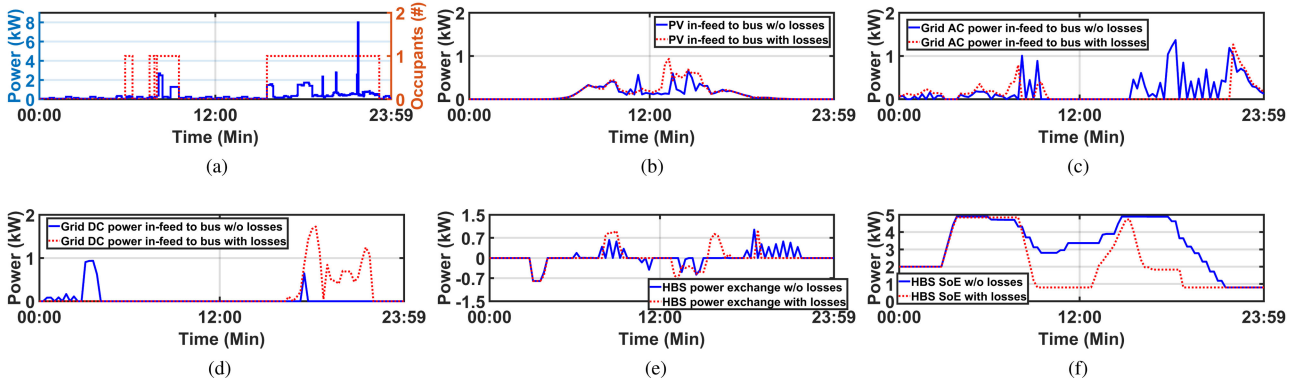
Fig. 5. AC/dc bus (w/o losses) versus ac/dc bus (with losses). (a) House occupants and their energy demands. (b) PV power in-feed. (c) Grid AC power in-feed. (d) Grid DC power in-feed. (e) HBS power exchange. (f) HBS state of energy.

TABLE II
SYSTEM PARAMETERS

Par:	Value	Par:	Value	Par:	Value
$S_{g.av}$	5 kVA	$\overline{P}_{pv.ac}$	1.05 kW	$\overline{E}_{b/gas}$	5 kWh
$\overline{P}_{b.dch}$	1.28 kW	$\overline{P}_{b.ch}$	0.8 kW	$P_{b.self}$	2 KW
$SoE_{initial}$	2 kWh	$\eta_{b.con}$	0.95	δ	0.8
$\underline{E}_{b/gas}$	2 KWh	$\eta_{inv}/\eta_{dc/ac}$	0.95	$\eta_{ac/dc}$	0.95
$C_{b.ivt}$	2000	ϕ	0.001	φ	0.0012
t	15 min	k	1 sec		

TABLE III
HOME APPLIANCES ACTIVITIES AND CLASSIFICATION

Activity	Appliance type	Mean cycle power (W)
Cooling	Refrigertaor	110
	Cassette / CD-player	15
	Hi-Fi	100
	Iron	1000
Consumer electronics	Personal computer	141
	Printer	335
	TV	124
	VCR / DVD	34
	TV receiver box	27
Cooking	Oven	2125
	Microwave	1250
	Kettel	2000
	Small cooking	1000
Wet	Dish wascher	1131
	Washing machine	406
Lighting	Bulbs	190

synchronous generators and modify the input power as a function of power, frequency, and voltage. To synchronize the system's phase angle, the phase-locked loop is used. Furthermore, L and R reflect the inductance and resistance between the VSI and the feeder bus forming an output filter. The local power control is always compatible with the voltage of the bus (i.e., $v^{gd} = V_{ac}$ and $v^{gq} = 0$) can be interpreted as

$$P = v^{gd}i^{gd}, \ Q = -v^{gd}i^{gq}. \tag{26}$$

It is also clear that the currents i^{gd} and i^{gq} will regulate the active and reactive force, as long as these currents track the current references i^{gd}_{ref} and i^{gq}_{ref}, respectively. Further dynamics of the VSI current controller can be expressed as [26]

$$V^d_{ac} = v^{gd} - \omega L i^{gq} + K^P(i^{gd}_{ref} - i^{gd}) + K^I \int (i^{gd}_{ref} - i^{gd}) \, dt \tag{27}$$

$$V^q_{ac} = v^{gq} - \omega L i^{gd} + K^P(i^{gq}_{ref} - i^{gq}) + K^I \int (i^{gq}_{ref} - i^{gq}) \, dt \tag{28}$$

where K^I and K^P are coefficients of the PI control.

IV. PERFORMANCE VALIDATION

To evaluate the performance of the scheduling algorithm and the real-time control strategy an architecture of ac/dc HAPN shown in Fig. 2 is used, along with proposed energy allocation scenarios. A case study from [2] is adapted that integrates electricity price indicators, load profiles, and solar radiation profiles. The parametric values of various power entities used are illustrated in Table II.

We also implemented a quantitative energy demand model that realizes the exact amount of energy needs for a single household energy usage. The estimated number of active inhabitants in

a household and their overall energy needs are shown in Fig. 5(a) with a time resolution of 1 min. Whereas the the list of commonly used power devices is illustrated in Table III.

Using optimization toolbox of "MATLAB," the optimization technique of MILP is used to obtain the optimal solution. A feasible solution (the minimum requirement of convergence guarantee) is sought using the MILP solver "intlinprog." The complexity of our dilemma is very immense, means

1) It has total of 12 binary and continuous optimization variables.
2) It has 3 linear equality constraints.
3) It uses 3 linear inequality constraints.
4) It uses 12 bounding condition constraints.

It takes 3 s for each iteration to take an integer solution to the necessary optimality stage. In this problem, the necessary degree of optimality is "integer feasible solution" and a relative gap of 0. The above investigation indicates that in the offline household appliances scheduling situation, it is promising to implement the suggested system.

Parameters		Scenario A	Scenario B	Scenario C	Scenario D
PV ulitization factor	(PV_{uf})	0.80	0.74	0.60	0.80
PV loss factor	(PV_{lf})	–	0.05	0.05	0.05
PV penetration level	(PV_{pl})	0.46	0.43	0.35	0.46
HBS ulitization factor	(HBS_{uf})	0.80	0.82	0.63	0.73
HBS loss factor	(HBS_{lf})	–	–	1.5	2.5
HBS penetration level	(HBS_{pl})	0.17	0.20	0.09	0.16
Grid ulitization factor	(G_{uf})	0.04	0.04	0.045	0.04
Grid loss factor	(G_{lf})	–	–	–	0.005
Grid penetration level	(G_{pl})	0.52	0.55	0.64	0.6
Inverter loss factor	(I_{lf})	–	–	–	0.00018

Parameters ("cent/day")		Scenario A	Scenario B	Scenario C	Scenario D
PV energy cost	(C_{pv})	31	29	24	31
HBS energy cost	(C_B)	14	16	7	13
HBS lifecyle loss cost	$(C_{b,l})$	2.7	2.8	2.7	2.5
Grid energy cost	(C_G)	202	204	240	221
Total energy cost	(C_{total})	250	252	274	268

A. Comparison Study for Power Scheduling Scenarios

In the first part of discussing results, we have created five different HAPN architectural scenarios to compare the results obtained from the scheduler. These scenarios are illustrated as follows:

1) A: AC bus without losses [1].
2) B: Hybrid ac/dc bus with PV losses [3].
3) C: Hybrid ac/dc bus with PV and HBS losses [2].
4) D: All in $Scenario\ C$ with additional converter losses.

A correlation is made based on cost estimation of utilizing energy from various ESEs. Moreover, we also observe the utilization factors and the penetration levels of various power generators in a HAPN. Hence, the previously mentioned scenarios A, B, C, and D are compared in Table IV and V.

Primarily, while looking into Table IV, the PV utilization factor is highest in $scenario\ D$. It is due to the utilization of the excess energy to compensate losses in converters as compared to other scenarios. The power losses in the system are mainly compensated by the dc subgrid. It is cheap to use PV and battery to supply power in comparison to energy obtained from the ac subgrid. While, the cost is relatively very high due to the utility grid in-feed, especially for power loss compensation. However, it is the lowest in $scenario\ C$ as there is no converter loss involved, and it is not so cheap to get supply from dc bus. Besides, it uses an ac bus when the utility grid energy prices are relatively lower. Moreover, the PV loss factor is almost the same for all the scenarios because the efficiency factor is constant for any given value of the power. Whereas the PV penetration level is highest in $scenario\ A$ and $scenario\ D$ indicates that most loads are supplied with PV source and it is lowest in $scenario\ C$.

In addition, HBS utilization factor is high in $scenario\ B$ followed by $scenario\ A$ as shown in Table IV. One of the reasons is that these scenarios did not take in the battery losses, so it is efficient to use a maximum of battery in these scenarios to supply power to the loads. In contrast, it is the lowest in $scenario\ C$ because the battery losses are considered. Furthermore, in $scenario\ D$, the battery losses are increasing again because it is cheap to use the battery to compensate converter

losses. So, as the utilization factor of HBS increases, the loss factor is also increased with it. Whereas the HBS penetration level is highest in $scenario\ B$ and lowest in $scenario\ C$. It may be the same case as the utilization factor.

Furthermore, the grid utilization factor is high in $scenario\ C$ because the power from the utility is cheap to use and also to charge the battery attached at dc bus. A little of which is used to compensate for the ac–dc converter losses. However, it is lower in other scenarios because the HBS and converter loss are neglected in those scenarios. The grid loss factor is increased with introducing converter losses as shown in $scenario\ D$. The penetration level is also increased with the utilization factor.

The ESEs cost analysis mainly depends on the utilization factor. Hence, if we look into Table V, we can see that the operational cost for PV source is high in $scenario\ D$ and $scenario\ A$ and lowest in $scenario\ C$. Similarly, the HBS operational cost is high in $scenario\ B$, while lowest in $scenario\ C$. Moreover, the battery life-cycle loss cost is highest in $scenario\ B$ because the battery is deeply charged, and according to the (22) the battery degradation accounts a lot in this scenario. While it is lowest in $scenario\ D$ involving lesser variations in battery state of energy (SoE). Power from grid costs higher in $scenario\ C$, where the grid penetration level is a bit higher than the rest of scenarios. In the end, while analyzing the overall operational costs and the component loss factors of the HAPN, we suggest the best architectural scenario operate with is $scenario\ D$.

Moreover, the graphical comparison of two extreme scenarios is illustrated in Fig. 5. It shows a comparison of two ac/dc topologies of a HAPN for lossless and lossy power network. $Scenario\ A$ has no loss while $scenario\ D$ includes all the losses. As shown in Fig. 5(b) the PV in-feed in both scenarios has the same trend for the whole day with little variations. However, the PV in-feed in $scenario\ A$ is more fluctuating as compared to $scenario\ D$. This is due to the additional power required to compensate for losses. Moreover, grid's ac in-feed is much higher in the network without losses as shown in Fig. 5(c). Because the combined in-feed from battery and PV is lower as compared to the network with losses. However, grid dc in-feed is opposite to it as demonstrated in Fig. 5(d). It is due to power loss compensation that is usually done by the dc bus. So, there is always room to charge the battery from ac power using ac–dc converter. In Fig. 5(e), the battery power exchange rates are quite similar following the same pattern. But power rates are more fluctuating in $scenario\ A$. Besides, the SoE of battery considering losses is more often lower indicating high utilization for power loss compensations.

The further analysis for $scenario\ D$ is shown in Fig. 6, indicating power utilization along with converter losses. This scenario is more realistic and practical in nature as it demonstrates the actual losses induced in the system due to the power flow through various converters. For example, in Fig. 6(a), the actual dispatched power from the PV module is always less than the power obtained from the PV array. It is because of the losses induced by the dc/dc converter attached to the PV array for MPPT operation purposes. The converter efficiency is suggested to be around 0.95 [2]. The zoom-in figure shows the clear picture
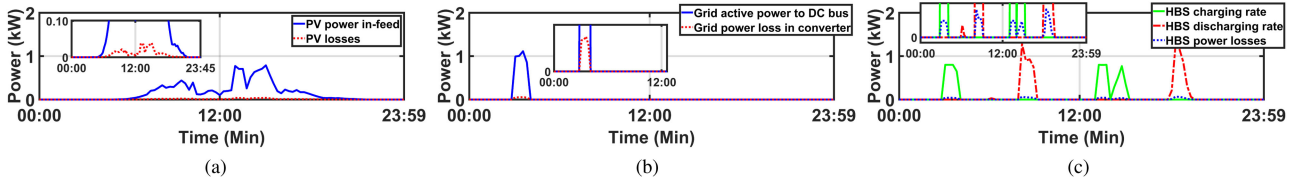
Fig. 6.   Hybrid ac/dc bus with losses. (a) PV power and losses. (b) Grid DC power and losses. (c) HBS power exchange and losses.

TABLE VI
COMMUNICATION SYSTEM PARAMETERS

Model Parameters		Channel Parameters	
Distance within Tx & Rx	3 m	Breakpoint distance	10 m
Carrier frequency	5.25e9 Hz	RMS delay spread	50 ns
Channel bandwidth	20 MHz	Maximum delay	390 ns
Modulation	16-QAM	Rician K-factor	3 dB
Noise model	AWGN	Number of clusters	3
SNR	28 dB	Number of taps	18
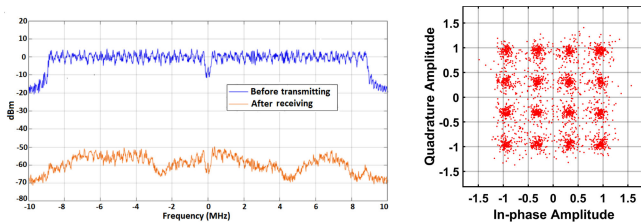
Fig. 7.   Frequency spectrum and data symbols output.

Fig. 8.   Master slave communication experimental setup.

Fig. 9.   Time-triggered communication setup between nodes.

of the losses induced with the actual power obtained from the PV module.

Furthermore, the utility grid power contribution to the dc bus is shown in Fig. 6(b). As illustrated in Fig. 2, the ac supply is attached to the dc bus through an ac/dc converter, which exhibits an inefficiency of 0.5. Therefore, during power transfer, one can see these power losses. This power transfer is usually activated when the utility grid energy price is relatively at its minimum and the batteries are being charged exploiting this benefit in off-peak times.

In addition, the simulation for power exchange through the battery is shown in Fig. 6(c). The charging and discharging rates are activated alternatively according to (2). The efficiency factor of a battery is already discussed in (1), which is the combination of losses of the converter and the battery itself. The battery may experience losses during both charging and discharging operations. These losses are shown more clearly in the zoomed window of the figure. Moreover, an inverter is placed between dc and ac bus to supply the power from dc energy sources (i.e., Battery and PV array) to the ac loads. This inverter is capable of providing power to the load side. As described in Section II, that during power transfer the inverter exhibits some power losses, which could possibly be released in the form of heat.
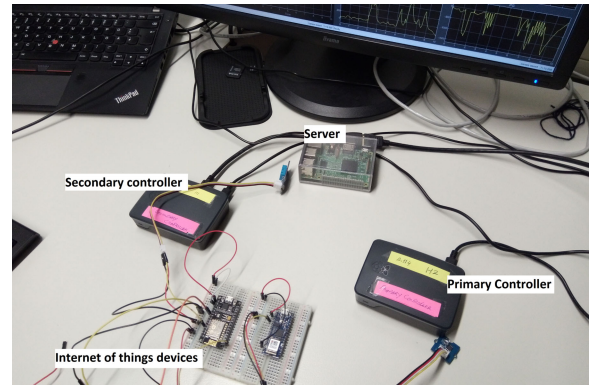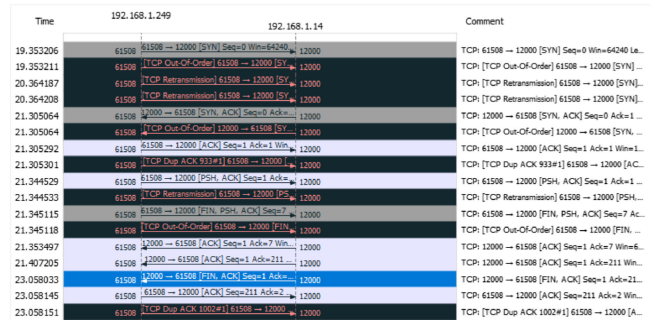
B. Communication Link Performance Parameters and Experimental Setup

The parameters of the communication system under investigation are given in Table VI.

Furthermore, the signal strength is evaluated by the signal-to-noise ratio (SNR). It affects the system's output [e.g., the signal strength gets lower if SNR reduces increasing bit error rate (BER)] and declines the sensitivity. Fig. 7(a) shows the difference of SNR in transmitted and received signal or can be perceived as a path loss that accounts for about 50 to 60 dB of segregation among the waveforms before and after it passes through the communication channel. This path loss originates because of the distance of 3 m between the transmitter and receiver incorporating shadowing effects and AWGN noise. The received signal level deviations indicate the frequency selectivity of the channel delay profile across the frequency spectrum. The
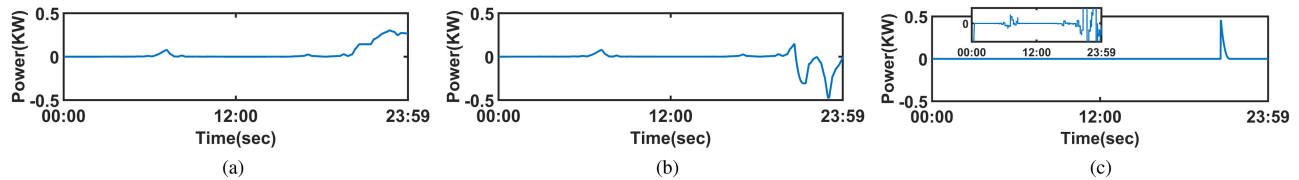
Fig. 10.   Real-time HAPN operation. (a) Load demand uncertainty. (b) Grid auxiliary storage power exchange. (c) System balancing.

SNR ratio we calculated for good communication is 28 dB. Below this SNR value, the probability of error goes higher.

Moreover, the equalized data symbols for each packet processed are displayed in Fig. 7(b). The figure shows the constellation of the equalized symbols at the output. It indicates the midpoint of each QAM constellation is almost with no error and the red dots around the midpoint depict the analytical position of each data point with noise. The less spreading (lower range of constellation spread) of these data points indicates low bit error rates. Increasing the channel noise may cause to spread of the distinct constellation points resulting in elevating error rates. In this work, a total of 1.416×10^{09} packets are generated and transmitted over a period of 24 h. In the current design, we have used raspberry pi as master (secondary controller) and slave (primary controller) nodes and have implemented a communication channel between them as shown in Fig. 8. One of the raspberry pi acts as a slave collecting information from the devices/sensors (i.e., internet of things) and acts as a local primary controller to control those devices. Whereas the other one acts as a scheduler generating optimal control signals. The existing infrastructure of the network stack in the Linux operating system of raspberry pi is used for communication. In this case, TCP with underlying IP as a network layer is used. The decision is made based on the priority of data integrity over speed. Besides, we have planned to make use of the existing internet infrastructure. Because of these reasons TCP/IP was used for communication between the master and slave nodes. Moreover, the master–slave communication between two nodes can be seen in Fig. 9. The decision of choosing TCP/IP is also justified here as no packet is lost and all the packets, which are lost are retransmitted. The data transmitted from the secondary controller and received at the primary controller is evaluated with good accuracy.

C. Power Sharing During Communication Failure and Load Uncertainties

A Simulink model of a NG presented in Fig. 1 is utilizes to test the real-time control policy for *scenario D*. To address the load demand dynamics, an unforeseeable volatile load demand model composition is assimilated into the real-time power system as seen in Fig. 10(a). To preserve the power balance of the energy network auxiliary storage is attached, which looks after any imbalance in the system resulting from the unforeseen changes in the solar power output, the load demands, or the loss of signal from the scheduler. Finally, in the previously expected load demand model, a load interruption model is consolidated.

For instance, the foretold power load is disengaged for 3600 s at 20 h of the day possibly due to the communication interruption. This phenomenon models an uncertain situation for a primary controller to handle with immediate action. The GAS deals with both the load addition and the load discontinuity. As seen in Fig. 10(b), it acts as a buffer that absorbs additional energy in the system and adds energy while the system is lower in energy.

There are some power spikes visible in Fig. 10(c) demonstrates the start of power network asymmetry. The auxiliary storage fixes the irregularity in a timely manner by adding extra power during the night while the load is disconnected. During load disruption and ambivalence, the ESEs are still programmed to supply energy in compliance with the scheduler management decision. The GAS is therefore remunerating the expected imbalance energy. Here, it is worth specifying that the HAPN could be directly balanced by the grid. However, massive on-demand energy prices can increase the cost to the customer. Insignificant differences in the zoomed pane of Fig. 10(c) show the chattering effect induced by the action of the controller.

V. CONCLUSION

This work presents a rolling horizon-based time-trigged scheduling and distributed coordinated control for power sharing in a hybrid ac/dc HAPN. A novel three-layered multitime scale HEMS is introduced. For different dispatchable ESEs using a MILP-based approach, the suggested secondary control scheduler offers the optimum cost scheduling decision vector. The wirelessly distributed decision signals to the local device level control are influenced by additive noise and restricted bandwidth limits. Besides, the signals received at the local primary controller are used as a reference value for operating the target physical device using power electronics. The robust control strategy employing proportional and integral control guarantees the tracking of those reference signals. Furthermore, during signal loss or power imbalance, a distributed coordinated control successfully achieves the power sharing utilizing grid auxiliary reserve power source by autonomously compensating the imbalance. A comparative analysis of various HAPN architectural scenarios shows the impact of losses on overall energy cost. In addition, through MATLAB/SimPowerSystems, the output of the proposed control strategy is validated. We will concentrate on extending this work to multiagent control framework at the microgrid level in our further work. For both offline scheduling and online robust control mechanisms, we would also like to introduce hybrid time/event-triggered communication schemes.

REFERENCES

[1] D. M. Minhas and G. Frey, "Two-stage multi-time scale energy management control framework for home area power network," in *Proc. IEEE Int. Conf. Environ. Elect. Eng. IEEE Ind. Commercial Power Syst. Europe*, Jun. 2020, pp. 1–6.

[2] D. M. Minhas and G. Frey, "Modeling and optimizing energy supply and demand in home area power network (HAPN)," *IEEE Access*, vol. 8, pp. 2052–2072, 2020.

[3] H. Qiu, W. Gu, Y. Xu, and B. Zhao, "Multi-time-scale rolling optimal dispatch for AC/DC hybrid microgrids with day-ahead distributionally robust scheduling," *IEEE Trans. Sustain. Energy*, vol. 10, no. 4, pp. 1653–1663, Oct. 2019.

[4] B. Zhao, H. Qiu, R. Qin, X. Zhang, W. Gu, and C. Wang, "Robust optimal dispatch of AC/DC hybrid microgrids considering generation and load uncertainties and energy storage loss," *IEEE Trans. Power Syst.*, vol. 33, no. 6, pp. 5945–5957, Nov. 2018.

[5] M. Manbachi and M. Ordonez, "Intelligent agent-based energy management system for islanded ac-dc microgrids," *IEEE Trans. Ind. Informat.*, vol. 16, no. 7, pp. 4603–4614, Jul. 2020.

[6] S. Singh, V. B. Pamshetti, and S. P. Singh, "Time horizon-based model predictive volt/var optimization for smart grid enabled CVR in the presence of electric vehicle charging loads," *IEEE Trans. Ind. Appl.*, vol. 55, no. 6, pp. 5502–5513, Nov. 2019.

[7] P. J. Hart, R. H. Lasseter, and T. M. Jahns, "Coherency identification and aggregation in grid-forming droop-controlled inverter networks," *IEEE Trans. Ind. Appl.*, vol. 55, no. 3, pp. 2219–2231, May 2019.

[8] Q. Zhou, M. Shahidehpour, A. Paaso, S. Bahramirad, A. Alabdulwahab, and A. Abusorrah, "Distributed control and communication strategies in networked microgrids," *IEEE Commun. Surv. Tut.*, vol. 22, no. 4, pp. 2586–2633, Oct.–Dec. 2020.

[9] J. Lai, X. Lu, X. Yu, W. Yao, J. Wen, and S. Cheng, "Distributed multi-DER cooperative control for master-slave-organized microgrid networks with limited communication bandwidth," *IEEE Trans. Ind. Informat.*, vol. 15, no. 6, pp. 3443–3456, Jun. 2019.

[10] J. Peng, B. Fan, H. Xu, and W. Liu, "Discrete-time self-triggered control of DC microgrids with data dropouts and communication delays," *IEEE Trans. Smart Grid*, vol. 11, no. 6, pp. 4626–4636, Nov. 2020.

[11] X. Lu, X. Yu, J. Lai, J. M. Guerrero, and H. Zhou, "Distributed secondary voltage and frequency control for islanded microgrids with uncertain communication links," *IEEE Trans. Ind. Informat.*, vol. 13, no. 2, pp. 448–460, Apr. 2017.

[12] X. Lu, J. Lai, X. Yu, Y. Wang, and J. M. Guerrero, "Distributed coordination of islanded microgrid clusters using a two-layer intermittent communication network," *IEEE Trans. Ind. Informat.*, vol. 14, no. 9, pp. 3956–3969, Sep. 2018.

[13] J. Lai, X. Lu, X. Yu, A. Monti, and H. Zhou, "Distributed voltage regulation for cyber-physical microgrids with coupling delays and slow switching topologies," *IEEE Trans. Syst., Man, Cybern. Syst.*, vol. 50, no. 1, pp. 100–110, Jan. 2020.

[14] J. Lai, X. Lu, X. Yu, and A. Monti, "Stochastic distributed secondary control for AC microgrids via event-triggered communication," *IEEE Trans. Smart Grid*, vol. 11, no. 4, pp. 2746–2759, Jul. 2020.

[15] Y. Xie and Z. Lin, "Distributed event-triggered secondary voltage control for microgrids with time delay," *IEEE Trans. Syst., Man, Cybern. Syst.*, vol. 49, no. 8, pp. 1582–1591, Aug. 2019.

[16] S. Liu, W. Luo, and L. Wu, "Co-design of distributed model-based control and event-triggering scheme for load frequency regulation in smart grids," *IEEE Trans. Syst., Man, Cybern. Syst.*, vol. 50, no. 9, pp. 3311–3319, Sep. 2020.

[17] P. Chen, L. Yu, and D. Zhang, "Event-triggered sliding mode control of power systems with communication delay and sensor faults," *IEEE Trans. Circuits Syst. I, Regular Papers*, vol. 68, no. 2, pp. 797–807, Feb. 2021.

[18] X. Lv, Y. Sun, Y. Wang, and V. Dinavahi, "Adaptive event-triggered load frequency control of multi-area power systems under networked environment via sliding mode control," *IEEE Access*, vol. 8, pp. 86585–86594, 2020.

[19] Y. Feng, W. Zhang, J. Xiong, and H. Li, "Distributed event-triggered communication scheme for economic dispatch problem in power system with uncoordinated step-sizes," *IEEE Access*, vol. 8, pp. 43 466–43 475, 2020.

[20] A. Wang, B. Mu, and Y. Shi, "Event-triggered consensus control for multiagent systems with time-varying communication and event-detecting delays," *IEEE Trans. Control Syst. Technol.*, vol. 27, no. 2, pp. 507–515, Mar. 2019.

[21] S. Linsenmayer, B. W. Carabelli, S. Wildhagen, K. Rothermel, and F. Allgower, "Controller and triggering mechanism co-design for control over time-slotted networks," *IEEE Control Netw. Syst.*, vol. 8, no. 1, pp. 222–232, Mar. 2021.

[22] A. Verma, B. Singh, A. Chandra, and K. A. Haddad, "An implementation of solar PV array based multifunctional EV charger," *IEEE Trans. Ind. Appl.*, vol. 56, no. 4, pp. 4166-4178, Jul.–Aug. 2020.

[23] D. M. Minhas, R. R. Khalid, and G. Frey, "Short term load forecasting using hybrid adaptive fuzzy neural system: The performance evaluation," in *Proc. IEEE PES PowerAfrica*, Jun.2017, pp. 468–473.

[24] X. Xu, Y. Jia, Y. Xu, Z. Xu, S. Chai, and C. S. Lai, "A multi-agent reinforcement learning based data-driven method for home energy management," *IEEE Trans. Smart Grid*, vol. 11, no. 4, pp. 3201–3211, Jul. 2020.

[25] L. He, Y. Li, J. M. Guerrero, and Y. Cao, "A comprehensive inertial control strategy for hybrid AC/DC microgrid with distributed generations," *IEEE Trans. Smart Grid*, vol. 11, no. 2, pp. 1737–1747, Mar. 2020.

[26] J. Lai, X. Lu, A. Monti, and R. W. D. Doncker, "Event-driven distributed active and reactive power dispatch for CCVSI-based distributed generators in AC microgrids," *IEEE Trans. Ind. Appl.*, vol. 56, no. 3, pp. 3125–3136, May 2020.

[27] D. I. Brandao, R. P. dos Santos, W. Silva, T. R. D. Oliveira, and P. F. Donoso-Garcia, "Model-free energy management system for hybrid AC/DC microgrids," *IEEE Trans. Ind. Electron.*, vol. 68, no. 5, pp. 3982–3991, May 2021.

[28] C. Li, S. Miao, D. Zhang, and L. Li, "A two-stage reactive power optimization strategy for AC/DC hybrid distribution network," in *Proc. 5th Asia Conf. Power Elect. Eng.*, Jun. 2020, pp. 426–431.

[29] C. Gray, R. Ayre, K. Hinton, and L. Campbell, "Smart is not free: Energy consumption of consumer home automation systems," *IEEE Trans. Consum. Electron.*, vol. 66, no. 1, pp. 87–95, Feb. 2020.

[30] B. Zhao, X. Zhang, J. Chen, C. Wang, and L. Guo, "Operation optimization of standalone microgrids considering lifetime characteristics of battery energy storage system," *IEEE Trans. Sustain. Energy*, vol. 4, no. 4, pp. 934–943, Oct. 2013.

[31] D. P. Jenkins, J. Fletcher, and D. Kane, "Lifetime prediction and sizing of lead-acid batteries for microgeneration storage applications," *IET Renew. Power Gener.*, vol. 2, no. 3, pp. 191–200, Sep. 2008.

[32] "Epexspot market data intraday auction," Dec. 2018. [Online]. Available: http://www.epexspot.com/en/market-data/intradayauction/quarter-auction-table/2018-12-09/DE.

[33] B. Aksanli and T. S. Rosing, "Human behavior aware energy management in residential cyber-physical systems," *IEEE Trans. Emerg. Topics Comput.*, vol. 8, no. 1, pp. 45–57, Jan. 2020.

[34] C. Opathella, A. Elkasrawy, A. A. Mohamed, and B. Venkatesh, "Optimal scheduling of merchant-owned energy storage systems with multiple ancillary services," *IEEE Open Access J. Power Energy*, vol. 7, pp. 31–40, 2020.

[35] S. Li, J. Yang, W. Song, and A. Chen, "A real-time electricity scheduling for residential home energy management," *IEEE Internet Things J.*, vol. 6, no. 2, pp. 2602–2611, Apr. 2019.

[36] I. Al-Anbagi, M. Erol-Kantarci, and H. T. Mouftah, "A low latency data transmission scheme for smart grid condition monitoring applications," in *Proc. IEEE Elect. Power Energy Conf.*, Oct. 2012, pp. 20–25.

[37] M. A. Ahmed, A. M. Eltamaly, M. A. Alotaibi, A. I. Alolah, and Y. Kim, "Wireless network architecture for cyber physical wind energy system," *IEEE Access*, vol. 8, pp. 40180–40197, 2020.

[38] Y. Xia, Y. Yu, P. Yang, Y. Peng, and W. Wei, "Generation-storage coordination for islanded dc microgrids dominated by pv generators," *IEEE Trans. Energy Convers.*, vol. 34, no. 1, pp. 130–138, Mar. 2019.

[39] N. Vazquez, S. S. Yu, T. K. Chau, T. Fernando, and H. H. Iu, "A fully decentralized adaptive droop optimization strategy for power loss minimization in microgrids with PV-bess," *IEEE Trans. Energy Convers.*, vol. 34, no. 1, pp. 385–395, Mar. 2019.